Model Predictive Direct Current Control: Formulation of the Stator Current Bounds and the Concept of the Switching Horizon

Tobias Geyer, *Senior Member, IEEE*

***Abstract*—A model predictive current controller for multi-level inverters driving electrical machines is proposed that keeps the stator currents within given bounds around their respective references and balances the inverter's neutral point potential around zero. The inverter switch positions are directly set by the controller, thus avoiding the use of a modulator. Admissible switching sequences are enumerated, and a state-space model of the drive is used to predict the drive's response to each sequence. The predicted short-term switching losses are evaluated and minimized. The concept of extrapolation and the use of bounds achieve an effective prediction horizon of up to 100 time-steps despite the short switching horizon. When compared to classic modulation schemes such as pulse width modulation, for long prediction horizons, the switching losses and/or the harmonic distortion of the current are almost halved when operating at low pulse numbers, thus effectively resembling the steady-state performance of optimized pulse patterns. During transients, the dynamic response time of the proposed controller is in the range of a few ms and thus very fast.**

***Index Terms*—AC motor drives, model predictive control, optimal control, direct current control**

I. Introduction

In high power applications exceeding one megawatt multi-level (rather than two-level) inverters are typically used, in order to reduce the rating of the semiconductor switching devices, to minimize the harmonic distortions and to increase the modulated voltage [1], [2]. The inverter must be operated in such a way that the desired three-phase load currents are produced. Several control methodologies are available to address this current control problem in three-phase voltage source inverters. As shown in the survey paper [3], the controllers can be grouped into linear and nonlinear control schemes.

The most prominent representative of the linear controller domain is Field Oriented Control (FOC), which is formulated in a rotating orthogonal reference frame [4]. Two (orthogonal) control loops are used, typically with Proportional Integral (PI) controllers augmented with feedforward terms—one for the torque producing and one for the flux producing current. A subsequent Pulse Width or Space Vector Modulator (PWM or SVM) translates the stator voltage reference signals into gating commands for the inverter [5]. Examples of nonlinear current control schemes include hysteresis controllers, which typically directly set the inverter switch positions. In a drive setting, the current control loop typically constitutes the inner loop within a cascaded control loop. On the machine side, the outer loop includes the torque and/or speed and the flux control loops, while on the grid side, the active and reactive power is controlled.

Recently, the power electronics community has started to investigate the concept of Model Predictive Control (MPC) [6], [7]. The roots of MPC can be traced back to the process industry, where the origins of MPC were developed in the 1970s [8]. The emerging field of MPC for three-phase voltage source inverters can be divided into two categories. The first one builds on FOC and replaces the inner (current) control loop by MPC and keeps the modulator in place. Examples of this approach include [9] and [10]. In the second variety, MPC directly manipulates the inverter switch positions, thus superseding a modulator. For Neutral Point Clamped (NPC) inverters, the latter scheme is available with a prediction horizon of one, as introduced in [11].

This paper proposes an MPC-based model predictive current controller with very long prediction horizons in the range of 100 time-steps. Specifically, a Model Predictive Direct Current Controller (MPDCC) for multi-level inverters is proposed that keeps the stator currents within specified bounds around their references, balances the inverter's neutral point potential(s) around zero and minimizes either the inverter switching losses or its switching frequency. The control problem is formulated in an orthogonal reference frame, which can be either stationary or synchronously rotating. A modulator is not required, since the gating signals are directly synthesized by the controller.

The key benefit of this approach is that both the current control and the modulation problems are addressed in one computational stage. As a result, the current harmonic distortion and the switching losses can be reduced at the same time, when compared to PWM. Indeed, at low switching frequencies, the resulting steady-state behavior is similar to the one obtained by Optimized Pulse Patterns (OPP) [12], [13]. During transients, however, a very fast current response time is achieved. This is in stark contrast to OPPs, which tend to be applicable only in very slow control loops.

This MPDCC scheme can be considered as an adaptation of Model Predictive Direct Torque Control (MPDTC) to the current control problem. This is achieved by changing the control objectives—namely, instead of controlling the torque and flux magnitude, the stator currents are controlled. MPDTC was developed in early 2004, see [7] and [14], with prediction horizons in the range of a few dozen time-steps, experimen-

T. Geyer is currently with the Department of Electrical and Computer Engineering, The University of Auckland, Private Bag 92019, Auckland 1142, New Zealand; tel. number: +64 (9) 373 7599 extension 89634; e-mail: t.geyer@ieee.org

A preliminary version of this paper was published and presented at the ECCE 2010 in Atlanta, USA, with the paper ID 974.

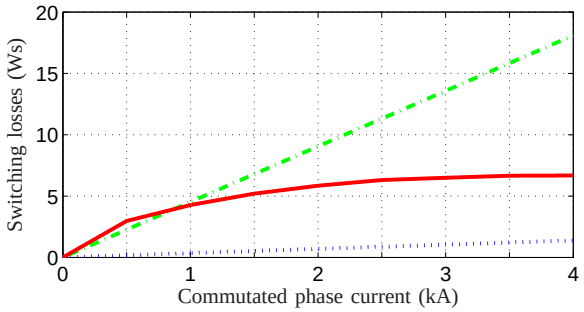

Fig. 1: Switching losses as a function of the commutated current for the GCT and the diodes. The GCT turn-on losses are indicated by the dotted blue line, the GCT turn-off losses by the dash-dotted green line, and the reverse recovery losses are the straight red line

tally verified on a 2.5 MVA drive in 2007 [15] and later generalized to enable even longer prediction horizons [16]. Preliminary results of an MPDCC scheme for a two-level inverter based on the initial MPDTC algorithm minimizing the inverter switching frequency and using relatively short prediction horizons were presented in [17].

II. Physical Model of the Drive System

Throughout this paper, we will use normalized quantities. Extending this to the time scale t, one time unit corresponds to $1/\omega_b$ seconds, where ω_b is the base angular velocity. Additionally, we will use $\xi(t)$, $t \in \mathbb{R}$, to denote continuous-time variables, and $\xi(k)$, $k \in \mathbb{N}$, to denote discrete-time variables.

A. The $\alpha\beta 0$ Reference Frame

All variables $\xi_{abc} = [\xi_a \ \xi_b \ \xi_c]^T$ in the three-phase system (abc) are transformed to $\xi_{\alpha\beta 0} = [\xi_\alpha \ \xi_\beta \ \xi_0]^T$ in the orthogonal $\alpha\beta 0$ stationary reference frame through $\xi_{\alpha\beta 0} = P\,\xi_{abc}$. Using the $\alpha\beta 0$ reference frame and aligning the α-axis with the a-axis, the following transformation matrix is obtained

$$P = \frac{2}{3}\begin{bmatrix} 1 & -\frac{1}{2} & -\frac{1}{2} \\ 0 & \frac{\sqrt{3}}{2} & -\frac{\sqrt{3}}{2} \\ \frac{1}{2} & \frac{1}{2} & \frac{1}{2} \end{bmatrix} . \tag{1}$$

B. Physical Model of the Inverter

As an illustrative example for a variable speed drive system with a multi-level inverter, consider a three-level Neutral Point Clamped (NPC) voltage source inverter driving an induction machine, as depicted in Fig. 2. The total dc-link voltage V_{dc} over the two dc-link capacitors x_c is assumed to be constant. Let the integer variables u_a, u_b, $u_c \in \{-1, 0, 1\}$ denote the switch positions in each phase leg—the so called phase states, where the values $-1, 0, 1$ correspond to the phase voltages $-\frac{V_{\text{dc}}}{2}, 0, \frac{V_{\text{dc}}}{2}$, respectively. Note that in a three-level inverter 27 different switch combinations exist. The actual voltage applied to the machine terminals is given by $v_{\alpha\beta 0} = 0.5 V_{\text{dc}}\, P\, u_{abc}$ with $u_{abc} = [u_a \ u_b \ u_c]^T$.

The neutral point potential $v_n = 0.5(V_{\text{dc,lo}} - V_{\text{dc,up}})$ between the two capacitors floats. In here, $V_{\text{dc,lo}}$ and $V_{\text{dc,up}}$ denote the

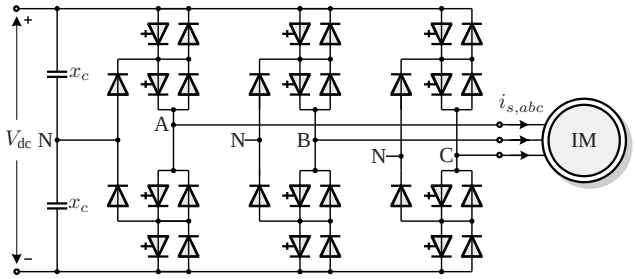

Fig. 2: Three-level neutral point clamped voltage source inverter driving an induction machine

voltage over the lower and upper dc-link half, respectively. The neutral point potential changes when current is drawn directly from it, i.e. when one of the switch positions is zero. Taking into account that the phase currents sum up to zero, i.e. $i_{sa} + i_{sb} + i_{sc} = 0$, it is straightforward to derive

$$\frac{dv_n}{dt} = \frac{1}{2x_c} |u_{abc}|^T\, P^{-1}\, i_{s,\alpha\beta 0}\,, \tag{2}$$

where $i_{s,\alpha\beta 0}$ is the stator current expressed in the stator reference frame and $|u_{abc}| = [|u_a| \ |u_b| \ |u_c|]^T$ is the componentwise absolute value of the inverter switch positions [7].

To avoid a shoot-through, direct switching between the upper and lower rails is prohibited.

Switching losses arise in the inverter when turning the semiconductors on or off and commutating the phase current. These losses depend on the applied voltage, the commutated current and the semiconductor characteristics. Considering Integrated Gate Commutated Thyristors (IGCT), with the GCT being the semiconductor switch, the switch-on and switch-off losses can be well approximated to be linear in the dc-link voltage and the phase current. Yet for diodes, the reverse recovery losses are linear in the voltage, but nonlinear in the commutated current.

Observing that in an NPC inverter, the voltage seen by each semiconductor is always half the total dc-link voltage V_{dc} leads to the following turn-on (energy) loss of the j-th GCT.

$$E_{j,\text{on}} = e_{\text{on}}\, \frac{1}{2} V_{\text{dc}}\, |i_{\text{ph}}|\,, \tag{3}$$

where e_{on} is a GCT specific coefficient and i_{ph} is the phase current. For the GCT turn-off and diode reverse recovery losses, similar equations can be derived.

As shown in [16], [18], by inspecting the phase leg topology and the commutation paths, the switching (energy) losses per phase transition can be derived. Since the commutation depends on the polarity of the phase current, the cases with positive and negative phase current need to be treated separately. Summing up the switching (energy) losses in the individual semiconductor devices (with the unit Ws) yields the total switching (energy) losses E_{sw}, and dividing them by the elapsed time yields the average switching (power) losses P_{sw} for the inverter (with the unit W).

Using the 35L4510 4.5 kV 4 kA IGCT and the 10H4520 fast recovery diode as examples both from ABB, the device switching losses as a function of the commutated current are

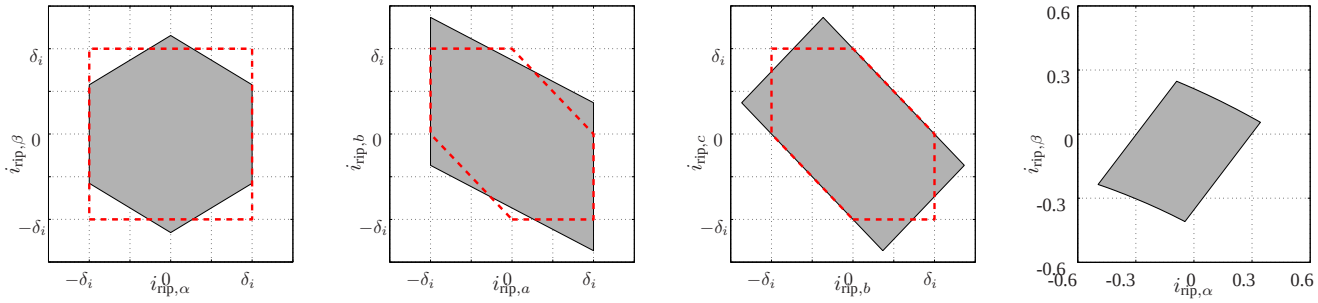

(a) Current ripple bounds in $\alpha\beta$ resulting from (7)

(b) Current ripple bounds in ab and ac resulting from (9)

(c) Current ripple bounds in bc resulting from (9)

(d) Torque and flux bounds translated into current ripple bounds in $\alpha\beta$

Fig. 3: Bounds on the current ripple in $\alpha\beta$, ab, ac and bc, when imposing current bounds in abc or in $\alpha\beta$, respectively. The right most figure shows the current ripple bounds in $\alpha\beta$, resulting from the torque and flux bounds imposed in model predictive direct torque control

depicted in Fig. 1, assuming $0.5V_{\text{dc}} = 2600\,\text{V}$ and a nominal operating temperature.

C. Physical Model of the Machine

The state-space model of a squirrel-cage induction machine in the stationary $\alpha\beta$ reference frame is summarized hereafter. For the current control problem at hand, it is convenient to choose the stator currents $i_{s\alpha}$ and $i_{s\beta}$ as state variables. The state vector is complemented by the rotor flux linkages $\psi_{r\alpha}$ and $\psi_{r\beta}$, and the rotor's angular velocity ω_r. The model input are the stator voltages v_α and v_β. The model parameters are the stator and rotor resistances r_s and r_r, the stator, rotor and mutual reactances x_{ls}, x_{lr} and x_m, respectively, the inertia J, and the mechanical load torque T_ℓ, where the rotor quantities are referred to the stator circuit.

The continuous-time state equations are [19], [20]

$$i_{s\alpha} + \tau_\sigma{}' \frac{di_{s\alpha}}{dt} = \frac{k_r}{r_\sigma \tau_r}\psi_{r\alpha} + \frac{k_r}{r_\sigma}\omega_r\psi_{r\beta} + \frac{1}{r_\sigma}v_\alpha \tag{4a}$$

$$i_{s\beta} + \tau_\sigma{}' \frac{di_{s\beta}}{dt} = \frac{k_r}{r_\sigma \tau_r}\psi_{r\beta} - \frac{k_r}{r_\sigma}\omega_r\psi_{r\alpha} + \frac{1}{r_\sigma}v_\beta \tag{4b}$$

$$\psi_{r\alpha} + \tau_r \frac{d\psi_{r\alpha}}{dt} = -\omega_r\tau_r\psi_{r\beta} + x_m i_{s\alpha} \tag{4c}$$

$$\psi_{r\beta} + \tau_r \frac{d\psi_{r\beta}}{dt} = \omega_r\tau_r\psi_{r\alpha} + x_m i_{s\beta} \tag{4d}$$

$$\tau_m \cdot \frac{d\omega_r}{dt} = T_e - T_\ell\,, \tag{4e}$$

with the electromagnetic torque

$$T_e = k_r(i_{s\beta}\psi_{r\alpha} - i_{s\alpha}\psi_{r\beta})\,. \tag{5}$$

The deduced parameters used in here are the coupling factor of the rotor $k_r = \frac{x_m}{x_r}$, the total leakage factor $\sigma = 1 - \frac{{x_m}^2}{x_s x_r}$, the equivalent resistance $r_\sigma = r_s + {k_r}^2 r_r$ and the leakage reactance $x_\sigma = \sigma x_s$, where $x_s = x_{ls} + x_m$ and $x_r = x_{lr} + x_m$. The deduced time constants include the transient stator time constant $\tau_\sigma{}' = \frac{\sigma x_s}{r_\sigma}$, the rotor time constant $\tau_r = \frac{x_r}{r_r}$ and the mechanical time constant $\tau_m = 1/J$.

Equations (4)–(5) represent the standard dynamical model of an induction motor, where the saturation of the machine's magnetic material, the changes of the rotor resistance due to the skin effect, and the temperature changes of the stator resistance are neglected.

III. Current Control Problem

The control problem is to regulate the stator currents around their references. During transients, a high dynamic performance is to be ensured, i.e. a short settling time in the range of a few ms. At steady state operating conditions, the harmonic distortion of the current is to be minimized, so as to reduce the copper losses and thus the thermal losses in the stator winding of the machine. The harmonic distortion of the current directly relates to the current ripple, which is defined as the deviation of the instantaneous current from its reference. Thus instead of reducing the current harmonic distortion, we can also minimize the ripple current. The proportionality between the ripple and the harmonic distortion will be shown in Sect. VI-C.

With regards to the inverter, the switching losses in the semiconductors are to be minimized. An indirect way of achieving this is to reduce the device switching frequency. The inverter's state(s), such as the neutral point potential, has to be balanced around zero.

A suitable measure for the harmonic distortion of the current is the Total Demand Distortion (TDD)

$$I_{\text{TDD}} = \frac{\sqrt{0.5\sum_{h\neq 0} I_h^2}}{I_{\text{nom}}}\,, \tag{6}$$

in which the nominal current I_{nom} refers to the operating condition at nominal speed and load of the drive. The (harmonic) Fourier components I_h, $h \geq 0$, can be differentiated into the fundamental current component I_0 and the h-th harmonic amplitude component I_h[1].

The TDD is a more suitable means to express the harmonic distortion than the Total Harmonic Distortion (THD), which is defined similarly to (6), but is referred to the fundamental of the present current rather than the nominal current. As a

[1]Note that the nominal current is an rms value, while the harmonic amplitudes are peak values. The factor 0.5 is required to translate these peak values into rms values. Moreover, the above definition holds for a single-phase current only. To compute the TDD of a three-phase current, the TDD is computed for each a, b and c current component separately, and the overall TDD is determined by taking the mean value of the three.

result, for small amplitudes of the fundamental current, the THD tends to go to infinity, while the TDD remains effectively constant.

The harmonic distortion of the electromagnetic torque is defined according to (6).

IV. Formulation of the Stator Current Bounds

The bounds on the stator currents can be imposed in various manners. Assume symmetric bounds around the current reference. Let δ_i denote the difference between the upper (lower) bound and the reference.

The natural choice [3] is to impose upper and lower bounds on the abc current of the form

$$|i_{\text{rip},a}| \leq \delta_i\,, \quad |i_{\text{rip},b}| \leq \delta_i\,, \quad |i_{\text{rip},c}| \leq \delta_i\,, \tag{7}$$

where the ripple current in phase a is defined as $i_{\text{rip},a} = i_{s,a} - i_{\text{ref},a}$. The ripple currents in phases b and c are defined accordingly. Using (1) and taking into account that the ripple currents are common mode free (the machine's star point is not connected), the constraints (7) can be translated from the abc into the $\alpha\beta$ frame.

$$|i_{\text{rip},\alpha}| \leq \delta_i\,, \quad |i_{\text{rip},\alpha}| + \sqrt{3}|i_{\text{rip},\beta}| \leq 2\delta_i \tag{8}$$

The set of ripple currents in $\alpha\beta$ that meet (7) is depicted in Fig. 3(a) as a gray polygon. The edges of the polygon are called facets. The facets are perpendicular to the a, b and c-axes, respectively. The distance of the facets to the origin is given by δ_i. The 0-component of the current ripple is always zero.

Conversely, one might impose upper and lower bounds on the currents in the $\alpha\beta$ frame, as proposed e.g. in [17].

$$|i_{\text{rip},\alpha}| \leq \delta_i\,, \quad |i_{\text{rip},\beta}| \leq \delta_i \tag{9}$$

This constraint is visualized in Fig. 3(a) as a square with dashed (red) lines. Translating the set imposed by (9) from $\alpha\beta$ to abc yields a non-trivial shape. Fig. 3(b) shows the set in an orthogonal plane, spanned by the a and b-axis. In the ac plane, this set is the same, while Fig. 3(c) shows the set in the bc plane. The polygons formed by the dashed (red) lines in Figs. 3(b) and 3(c) refer to the constraint (7).

It is obvious that the two constraint formulations (7) and (9) lead to different sets in $\alpha\beta$ and abc. The current harmonic distortion relates to the ripple in abc rather than in $\alpha\beta$. Thus, from a TDD perspective, it is advantageous to impose the constraint (7) rather than (9). This is confirmed by simulation results, even though the difference is fairly small, amounting only to a few percent. Since the machine model is formulated in $\alpha\beta$, it is convenient to formulate the current constraints also in this reference frame. Therefore, the constraint formulation (8), which is equivalent to (7), is adopted for MPDCC.

On the other hand, in a model predictive direct torque and flux control setting, i.e. MPDTC, the stator flux vector is the key figure to be controlled. Specifically, the angle between the stator and rotor flux vectors determines the electromagnetic torque, while the stator flux's magnitude is usually kept around its nominal value to keep the machine fully magnetized. By imposing upper and lower bounds on the torque and the stator flux magnitude, a target window results that defines the ripple of the stator flux vector. Due to the direct correspondence between the stator flux and the stator current, the stator flux's target window can be translated into an equivalent window for the stator current ripple in $\alpha\beta$. The latter is shown in Fig. 3(d). Particularly at high speed operation, the bounds on the stator flux magnitude tend to be asymmetric with respect to the desired average flux. Then, the set of ripple currents is also asymmetric with respect to the origin. The curvature results from the bounds on the stator flux magnitude. Note that in $\alpha\beta$, this window rotates around the origin.

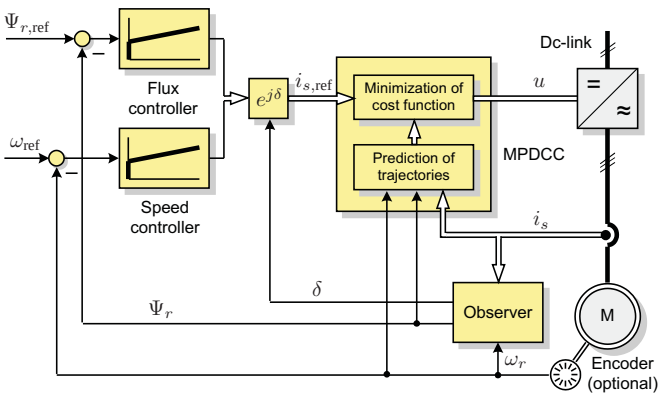

Fig. 4: Model predictive direct current control (MPDCC) for a multi-level voltage source inverter driving an electrical machine

V. Model Predictive Direct Current Control

As shown in Fig. 4, MPDCC constitutes the inner current control loop formulated in the stationary $\alpha\beta$ reference frame. The inverter switch positions are directly set by the controller, thus not requiring the use of a modulator. The current loop is augmented in a cascaded controller fashion by an outer loop that operates in the rotating dq frame and comprises a flux and a speed PI controller with feedforward terms.

A. Internal Controller Model

MPC relies on an internal model of the physical drive system to predict the future drive trajectories, specifically the current and neutral point trajectories.

The overall state vector of the drive is chosen to be $x = [i_{s\alpha}\ i_{s\beta}\ \psi_{r\alpha}\ \psi_{r\beta}\ v_n]^T$, the switch positions constitute the input vector $u = u_{abc} = [u_a\ u_b\ u_c]^T \in \{-1, 0, 1\}^3$, and the stator current along with the neutral point potential is the output vector $y = [i_{s\alpha}\ i_{s\beta}\ v_n]^T$. The rotor speed is assumed to be effectively constant within the prediction horizon, which turns the speed into a time-varying parameter. The prediction horizon being in the range of a few ms, this appears to be a mild assumption for medium-voltage drive applications. Nevertheless, including the speed as an additional state in the model might be necessary for highly dynamic drives and/or drives with a small inertia.

Combining the motor model (4)–(5) with the inverter model (2) and using the Euler formula, the following discrete-

time state-space model of the drive can be derived in accordance with [14].

$$x(k+1) = \big(I + \begin{bmatrix} A & 0 \\ 0 & 0 \end{bmatrix} T_s\big)x(k) + \tag{10a}$$
$$+ \begin{bmatrix} B_1 \\ 0 \end{bmatrix} T_s u(k) + \begin{bmatrix} 0 \\ B_2(x(k)) \end{bmatrix} T_s |u(k)|$$
$$y(k) = Cx(k) \tag{10b}$$

In this model, I denotes the identity matrix and $T_s = 25\,\mu$s is the sampling interval. The definitions of the matrices A, B_1, B_2 and C can be found in the appendix. The zeros in (10) are vectors and matrices of appropriate dimensions. In (10a) the first two terms capture the motor equations, while the third expression captures the dynamic of the neutral point potential.

B. MPC Optimization Problem

As stated in Sect. III, the control objectives are to keep the instantaneous stator current components within given bounds around their respective references and to balance the neutral point potential around zero, while minimizing the switching losses. These control objectives are mapped into an objective function that yields a scalar cost (here the short-term switching losses) that is minimized subject to the dynamical evolution of the internal prediction model of the drive system and subject to constraints. This leads to the following closed-form optimization problem.

$$J^*(x(k)) = \min_{U(k)} \frac{1}{N_p T_s} \sum_{\ell=k}^{k+N_p-1} E_{\text{sw}}(x(\ell), u(\ell), u(\ell-1)) \tag{11a}$$
$$\text{s.t. } x(\ell+1) = Ax(\ell) + Bu(\ell) \tag{11b}$$
$$y(\ell) = Cx(\ell) \tag{11c}$$
$$y(\ell) - y_{\text{ref}}(\ell) \in \mathcal{Y} \tag{11d}$$
$$u(\ell) \in \{-1, 0, 1\}^3, \max|\Delta u(\ell)| \leq 1 \tag{11e}$$
$$\forall \ell = k, \ldots, k+N_p-1 \tag{11f}$$

$J^*(x(k))$ denotes the minimum of the objective function J as a function of the state vector $x(k)$ at the current time-instant k. The sequence of control inputs $U(k) = [u(k), \ldots, u(k+N_p-1)]$ over the prediction horizon N_p represents the sequence of inverter switch positions the controller has to decide upon.

The objective function represents the sum of the switching energy losses over the prediction horizon divided by the length of the horizon in time—it thus approximates the short-term average switching power losses. Note that, according to (3), the instantaneous switching energy loss E_{sw} at time-instant ℓ is a function of the stator current $i_s(\ell)$, which is part of the state vector $x(\ell)$. E_{sw} also depends on the inverter switching transition at time-step ℓ, which can be deduced from $u(\ell)$ and $u(\ell-1)$. An indirect (and less effective) way of minimizing the switching losses is to minimize the number of commutations, i.e. the device switching frequency.

The objective function is minimized subject to the dynamical evolution of the drive system, represented in state-space form with the matrices A, B and C given in the appendix. The bounds on the output variables are imposed by the constraint (11d), with $y_{\text{ref}} = [i_{s\alpha,\text{ref}}\ i_{s\beta,\text{ref}}\ \upsilon_{n,\text{ref}}]^T$ denoting the reference of the output vector. Note that the latter is time-varying in $\alpha\beta$, but the reference trajectory can be approximated e.g. by a quadratic function. The set $\mathcal{Y}$ is given by the lower and upper bounds, i.e. $\mathcal{Y} = [-\delta_i, \delta_i] \times [-\delta_i, \delta_i] \times [-\delta_\upsilon, \delta_\upsilon]$, with the bound on the current ripple δ_i defined as previously, and δ_υ being the bound on the neutral point potential.

The constraint (11e) limits the control input u to the integer values $\{-1, 0, 1\}$ available for a three-level inverter. Switching between the upper and the lower rail is inhibited by the second constraint in (11e) with $\Delta u(\ell) = u(\ell) - u(\ell-1)$. These constraints have to be met at every time-step within the prediction horizon.

C. Simplified MPC Optimization Problem

Solving the closed-form optimization problem (11) is challenging from a computational point of view even for prediction horizons of modest length. Solving it for reasonably long horizons appears to be impossible, since this constitutes a mixed-integer programming problem. One attractive solution is to consider switching transitions only when the output ripple $y - y_{\text{ref}}$ is close to its bound $\mathcal{Y}$, i.e. when switching is imminently required to keep the outputs within their bounds. When the outputs are well within their bounds, the switch positions are frozen and switching is not considered. This is in line with the control objective (11a) and greatly reduces the number of switching sequences to be evaluated and thus the computational burden.

To achieve this, three key concepts were introduced in [7], [14], [16] that are adopted for MPDCC.

1) The formulation of the optimization problem in an *open form*. For every admissible switching sequence the corresponding output trajectories are computed forward in time.
2) Between the switching events, the output trajectories are computed using the model (11b) and (11c), to which we refer as an *extension* step, or they are extrapolated in an approximate manner, which is a so called *extrapolation* step. Typically, quadratic extrapolation is used, even though linear extrapolation is often sufficiently accurate, particularly at low speed. More elaborate extension methods are conceivable, as shown in [21].
3) The set of admissible switching sequences is controlled by the so called *switching horizon*, which is composed of the elements 'S' and 'E' that stand for 'switch' and 'extrapolate' (or more generally 'extend'), respectively. The element 'e' denotes an optional extrapolation or extension step.

It is important to distinguish between the *switching* horizon (number of switching instants within the horizon, i.e. the degrees of freedom) and the *prediction* horizon (number of

time-steps MPC looks into the future). Between the switching instants, the switch positions are frozen and the drive behavior is extrapolated until a hysteresis bound is hit. The concept of extrapolation gives rise to long prediction horizons (typically 30 to 100 time-steps), while the switching horizon is very short (usually one to three). For more details about the concept of the switching horizon and its elements 'S', 'E' and 'e', the reader is referred to [16].

Starting at the current time-step k, the MPDCC algorithm iteratively explores the tree of feasible switching sequences forward in time—for more details about this tree, please refer to [22]. At each intermediate step, all switching sequences must yield output trajectories that are either *feasible*, or *pointing in the proper direction*. We refer to these switching sequences as *candidate* sequences. Feasibility means that the output variable lies within its corresponding bounds; pointing in the proper direction refers to the case in which an output variable is not necessarily feasible, but the degree of the bound's violation decreases at every time-step within the switching horizon. The above conditions need to hold *componentwise*, i.e. for all three output variables[2].

To visualize this concept, consider the switching horizon 'eSESE' and the candidate switching sequence denoted by straight (blue) lines in Fig. 5. The corresponding output trajectories (abc ripple currents and neutral point potential) are shown accordingly as straight (blue) lines[3]. Starting at the present time-step k, after an (optional) extrapolation step 'e', the ripple current in phase c is predicted to hit its lower bound shortly after time-step $k+9$. This triggers a predicted switch transition at time-step $k+9$ in phase c, followed by an extrapolation segment, until one of the four output variables is predicted to hit a bound. At step $k+53$, phase a is predicted to switch in order to avoid the ripple current in phase a to violate its constraint. This transition constitutes the second switching event in the horizon, which is followed by another extrapolation step.

Another candidate switching sequence along with its output trajectories is indicated by dashed (red) lines. Switching is predicted to occur at time-steps $k+9$ and $k+11$. Even though more switch transitions are required here, the switching (power) losses for the dashed (red) switching sequence are lower due to two reasons. Firstly, the second candidate switching sequence is roughly twice as long as the first one. Thus the losses are depreciated over a longer prediction horizon. Secondly, as cannot be seen here, the a and b phase currents are relatively small, thus incurring only small switching (energy) losses.

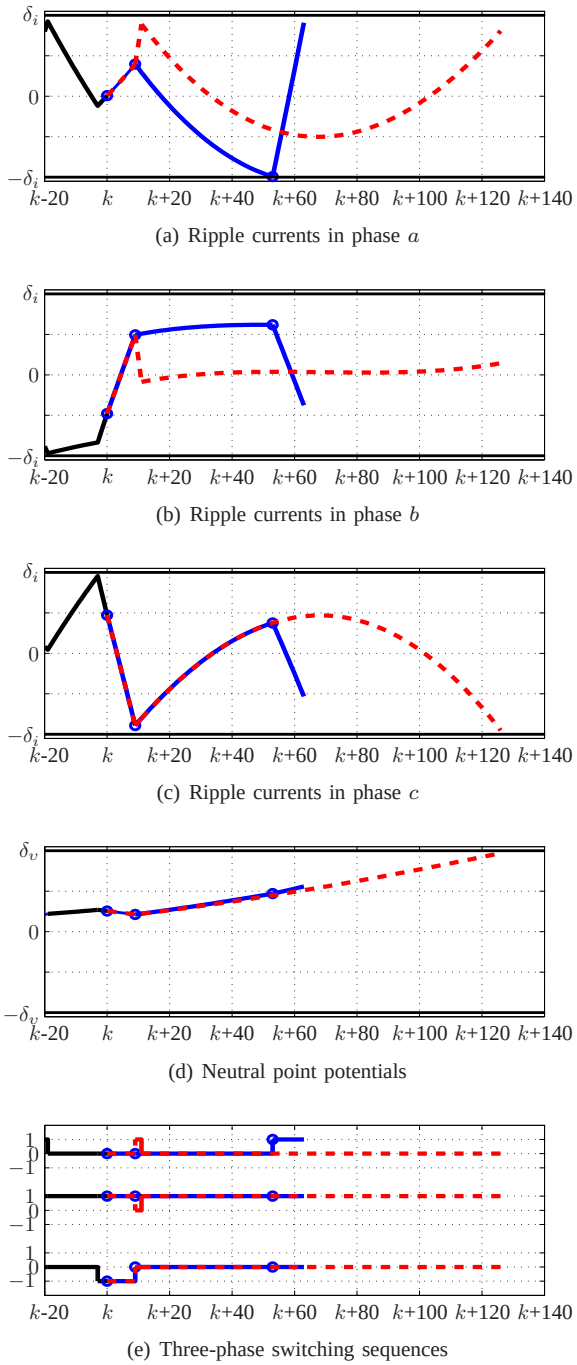

(a) Ripple currents in phase a

(b) Ripple currents in phase b

(c) Ripple currents in phase c

(d) Neutral point potentials

(e) Three-phase switching sequences

Fig. 5: Two candidate switching sequences with their associated three-phase ripple current trajectories as well as with their neutral point potential trajectories. These trajectories are constrained by their respective upper and lower bounds. The time-axis is given by the sampling instants with the sampling interval $T_s = 25\,\mu$s. The switching horizon 'eSESE' leads here to a prediction horizon of $N_p = 126$ time-steps or 3.15 ms

D. Generalized MPDCC Algorithm

The generalized MPDCC algorithm is based on a Last In First Out stack model, commonly used in computer science. At time-step k, the algorithm computes the three-phase switch position $u(k)$ according to the following procedure.

1) Initialize the root node with the current state vector

[2]As an example, consider the case where the α-current component is feasible, the β-current component points in the proper direction and the neutral point potential is feasible.

[3]Note that the MPDCC algorithm works with the $\alpha\beta$ rather than with the abc ripple currents, and it imposes the bounds (8). Since these bounds are difficult to visualize, the abc ripple currents are shown in Fig. 5 along with their corresponding upper and lower bounds.

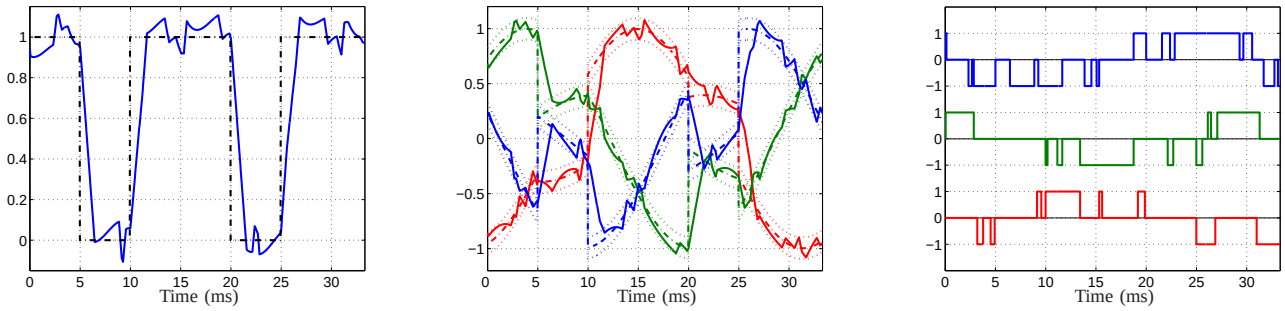

(a) Electromagnetic torque (b) Stator currents in abc (c) Switch positions in abc

Fig. 6: Dynamic response of model predictive direct current control during torque steps of magnitude 1 pu. The torque reference with the torque response, the three-phase stator currents and the switch positions are shown versus the time-axis in ms. The rotor's angular velocity is $\omega_r = 0.6$ pu, the current bound width is $\delta_i = 0.12$ and the switching horizon is 'eSESE'. The neutral point potential is not shown here

$x(k)$, the last switch position $u(k-1)$ and the switching horizon N_s, e.g. N_s ='SESE'. Push the root node onto the stack.

2a) Take the top node with a non-empty switching horizon $N_s \neq \emptyset$ from the stack.

2b) Read out the first element from N_s and remove it. For 'S', branch on all feasible switching transitions. For 'E', extend the trajectories either by extrapolation as detailed in [7], [21] or by using the internal controller model of Sect. V-A.

2c) Keep only the switching sequences that are candidates, i.e. sequences that yield output trajectories that are either feasible according to (11d) or pointing towards the bounds.

2d) Push these sequences onto the stack.

2e) Stop if there are no more nodes with non-empty switching horizons N_s. The result of this are the predicted (candidate) switching sequences $U^i(k) = [u^i(k), \ldots, u^i(k + n_i - 1)]$ over the variable-length prediction horizons n_i, where $i \in \mathcal{I}$ and $\mathcal{I}$ is an index set.

3) Compute for each (candidate) sequence $i \in \mathcal{I}$ the associated cost. If the switching frequency is to be minimized, consider the cost function $J_i = s_i/(n_i T_s)$, which approximates the average switching frequency, where $s_i = \sum_{\ell=k}^{k+n_i-1} ||u_i(\ell) - u_i(\ell-1)||_1$ is the total number of switch transitions in the switching sequence $U^i(k)$, and n_i is the corresponding sequence length. Conversely, if the switching losses are directly targeted, the cost function $J_i = E_{\text{sw},i}/(n_i T_s)$ is used, where $E_{\text{sw},i}$ is the sum of the device switching losses for the i-th switching sequence, according to Sect. II-B.

4) Choose the switching sequence $U^* = U^i(k)$ with the minimal cost, where $i = \arg\min_{i \in \mathcal{I}} c_i$.

5) Apply (only) the first switch position $u(k) = u^*$ of this sequence, and execute the above procedure at the next time-step $k + 1$ over a shifted horizon.

In the following, four remarks about the proposed MPDCC algorithm are provided to further clarify some of its important properties. Firstly, the MPDCC algorithm derives a long sequence of switch positions that minimizes the predicted inverter switching losses and is predicted to keep the output variables within their bounds. Out of this sequence, only the first gating signal (at the current time-instant) is applied to the inverter. At the next sampling instant, new measurements are obtained, the optimization step is repeated and a new switching sequence is computed. During steady-state operating conditions, this updated sequence is shifted in time by one step. In general, this sequence is also slightly modified in order to account for model mismatches, dc-link voltage fluctuations, measurement noise, observer errors, etc. This strategy, which is referred to as the receding horizon policy, provides feedback and makes MPDCC robust. When the current references are (significantly) changed, the switching sequence is completely revised.

Secondly, by adapting the drive model, MPDCC can also be formulated in a dq reference frame, rotating synchronously with the rotor. In dq, the current references are constant and so are the upper and lower bounds. However, the hexagon-shaped bounds, see Fig. 3(a), would rotate in the dq frame. A possible simplification would be to approximate the hexagon by a circle, similar to [23]. Moreover, in dq, the voltage vectors depend on the angular position of the frame, complicating the computation of the drive response in the MPDCC Step 2b.

Thirdly, the controller's computation time of one sampling interval has been neglected above. Using the internal controller model of the drive and the previously chosen switch position, this delay can be easily compensated by translating the measurements one time-step forward. For more details, see [15].

Fourthly, the bound width is the tuning parameter that sets the trade-off between the switching losses and the current distortion. For more details on how to tune MPDCC, see Sect. VI-C.

VI. Performance Evaluation

As a case study, consider a three-level NPC voltage source inverter driving an induction machine, as shown in Fig. 2. A 3.3 kV and 50 Hz squirrel-cage induction machine rated at 2 MVA is used as an example for a commonly used medium-voltage induction machine. The machine and inverter parame-

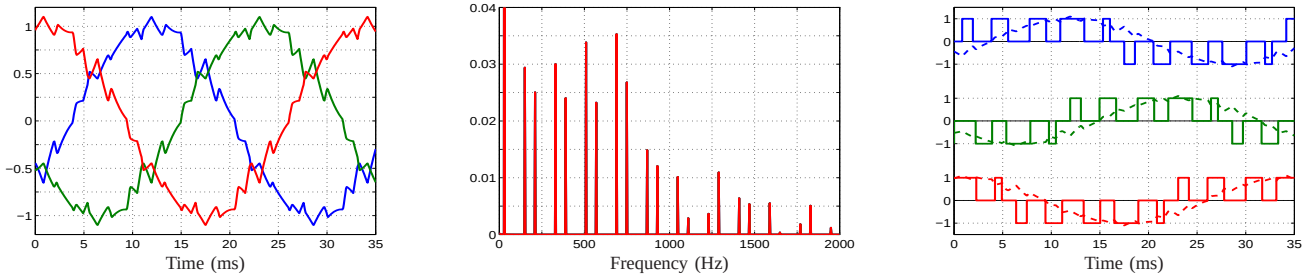

(a) Stator currents in abc (b) Stator current spectrum (c) Switch positions with stator currents

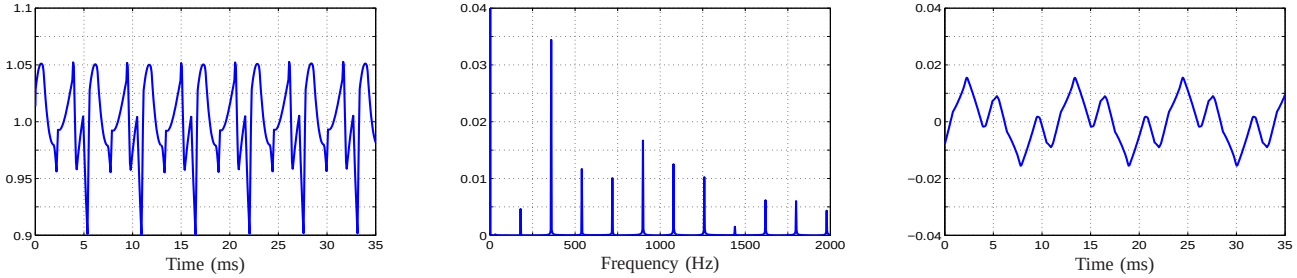

(d) Torque (e) Torque spectrum (f) Neutral point potential

Fig. 7: Field oriented control with PWM/SVM and the carrier frequency $f_c = 270\,\text{Hz}$ at 60% speed and full torque. The stator currents and the torque are shown in the time- and frequency-domain. The neutral point potential and the switch positions are shown versus the time-axis in ms. All quantities are given in pu

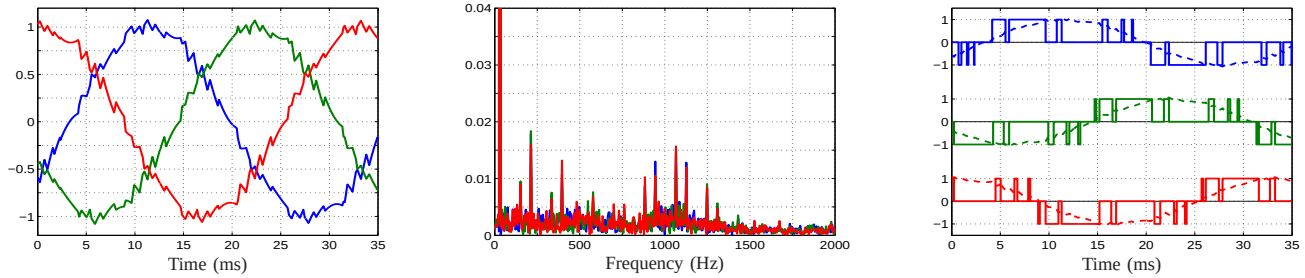

(a) Stator currents in abc (b) Stator current spectrum (c) Switch positions with stator currents

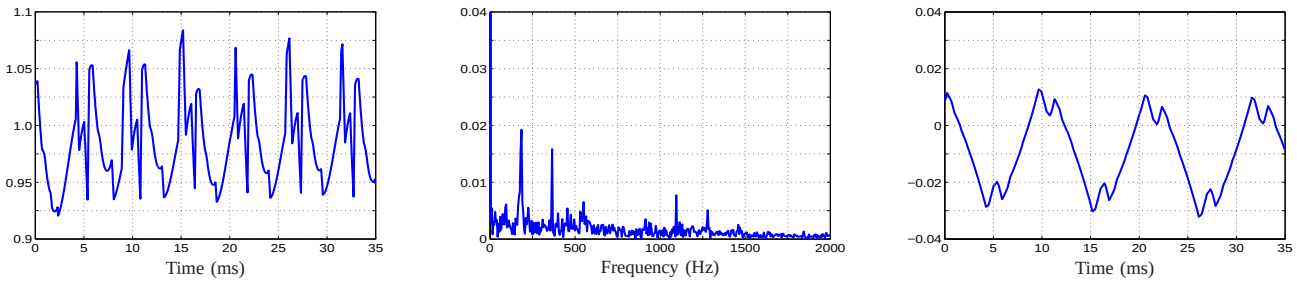

(d) Torque (e) Torque spectrum (f) Neutral point potential

Fig. 8: Model predictive direct current control (MPDCC) with the current bound $\delta_i = 0.086$. The switching horizon 'eSESESE' leads here to an average prediction horizon of 69 time-steps. The operating point, the plots and their scaling are the same as in Fig. 7 to facilitate a direct comparison

ters are summarized in Table I. The semiconductors used are ABB's 35L4510 4.5 kV 4 kA IGCT and ABB's 10H4520 fast recovery diode. The pu system is established using the base quantities $V_B = \sqrt{2/3}V_{\text{rat}} = 2694\,\text{V}$, $I_B = \sqrt{2}I_{\text{rat}} = 503.5\,\text{A}$ and $f_B = f_{\text{rat}} = 50\,\text{Hz}$. As previously, δ_i denotes the width of the bounds on the abc current components, which are symmetric around the reference, where δ_i is equal to the upper bound minus the reference.

A. Transients

At 60 % speed, torque reference steps of magnitude 1 pu are imposed. As shown in Fig. 6, a very fast current and thus torque response is achieved, limiting the length of the transients to about 1.5 ms. It is apparent from the control

Control scheme	Control setting	Switching horizon	Avg. prediction horizon N_p [steps]	P_{sw} [kW]	f_{sw} [Hz]	$I_{s,\text{TDD}}$ [%]	$T_{e,\text{TDD}}$ [%]	P_{sw} [%]	f_{sw} [%]	$I_{s,\text{TDD}}$ [%]	$T_{e,\text{TDD}}$ [%]
PWM/SVM	$f_c = 90\,\text{Hz}$	–	–	1.78	60.0	17.5	5.77	100	100	100	100
MPDCC	$\delta_i = 0.21$	eSE	63.2	1.00	61.0	10.7	5.09	56.2	102	60.8	88.2
OPP	$d = 2$	–	–	1.78	61.0	10.4	5.14	100	102	59.5	89.1
PWM/SVM	$f_c = 270\,\text{Hz}$	–	–	3.45	150	8.63	3.28	100	100	100	100
MPDCC	$\delta_i = 0.116$	eSE	23.6	3.43	192	8.23	6.67	99.4	128	95.4	203
MPDCC	$\delta_i = 0.096$	eSESE	51.1	3.50	187	6.36	4.12	101	125	73.7	126
MPDCC	$\delta_i = 0.086$	eSESESE	69.0	3.48	205	5.53	3.57	101	137	64.1	109
OPP	$d = 5$	–	–	3.73	152	5.57	3.02	108	101	64.5	92.1
PWM/SVM	$f_c = 720\,\text{Hz}$	–	–	8.84	375	3.13	1.33	100	100	100	100
MPDCC	$\delta_i = 0.048$	eSE	10.8	8.71	412	3.26	2.41	98.5	110	104	181
MPDCC	$\delta_i = 0.042$	eSESE	21.8	8.70	441	2.71	1.77	98.4	118	86.6	133
MPDCC	$\delta_i = 0.039$	eSESESE	29.8	8.78	505	2.52	1.69	99.3	135	80.5	127
OPP	$d = 12$	–	–	8.54	365	2.92	1.19	96.7	97.3	93.3	89.5

TABLE II: Comparison of MPDCC with PWM/SVM and OPP in terms of switching losses P_{sw}, switching frequency f_{sw}, current TDD $I_{s,\text{TDD}}$ and torque TDD $T_{e,\text{TDD}}$. The center part shows absolute values, while the values in the right part are relative using PWM as a baseline. The three sets of comparisons refer to a switching frequency of about 60 Hz, and switching losses of around 3.5 and 8.8 kW. The operating point is at 60% speed and nominal torque

algorithm described in Sect. V that MPDCC is similarly fast as deadbeat and hysteresis control schemes. Note that excessive switching during the transients is avoided, as can be seen from Fig. 6(c).

B. Steady-State Operation

At 60% speed and full torque, closed-loop simulations were run to evaluate MPDCC's performance at steady-state operating conditions. The key performance criteria here are the harmonic distortions of the current and the torque, and the switching losses in the inverter. This performance evaluation is done for switching horizons of varying length and for various bounds. MPDCC is compared with two well-established modulation methods: PWM/SVM and optimized pulse patterns (OPP).

Specifically, a three-level regular sampled PWM is used with two triangular carriers, which are in phase (phase disposition). It is generally accepted that for multi-level inverters carrier-based PWM with phase disposition (PD) results in the lowest harmonic distortion. As shown in [24]—by adding a proper common mode voltage to the reference voltage, which is of the min/max type plus a modulus operation—PWM with PD is equivalent to SVM, in the sense that both methods yield the same gating signals.

Alternatively, optimized pulse patterns can be calculated in an off-line procedure by computing the optimal switching angles over one fundamental period for all possible operating points [13], by minimizing the current distortion for a given switching frequency (pulse number). OPPs are typically used in a very slow control loop like V/f control, which is also employed here for the OPPs.

Induction Motor			
Voltage	3300 V	r_s	0.0108 pu
Current	356 A	r_r	0.0091 pu
Real power	1.587 MW	x_{ls}	0.1493 pu
Apparent power	2.035 MVA	x_{lr}	0.1104 pu
Frequency	50 Hz	x_m	2.3489 pu
Rotational speed	596 rpm		
Inverter			
Dc-link voltage	5200 V	V_{dc}	1.930 pu
		x_c	11.769 pu

TABLE I: Rated values (left) and parameters (right) of the drive

As shown in Fig. 7, PWM/SVM with the carrier frequency $f_c = 270\,\text{Hz}$ leads to distinctive current and torque spectra around multiples of f_c. The switching pattern is fairly uniformly distributed over a fundamental period. The resulting switching losses are 3.45 kW and the current TDD is 8.63%, as summarized in Table II. The MPDCC bounds are tuned such that similar switching losses are obtained—more details about the tuning of MPDCC can be found in Sect. VI-C. As the switching horizon is increased, the average prediction horizon increases, too, allowing MPDCC to make better informed decision by looking further into the future. As a result, the bounds can be tightened and thus the harmonic distortions of the current and the torque are reduced, whilst keeping the switching losses constant. This can be seen in Fig. 8, which shows the results for MPDCC with a long switching horizon and fairly tight bounds. For the same switching losses, the current distortion is reduced by 36%, while the torque distortion is not dissimilar. The switching frequency, however, tends to be higher than in PWM, since it is not directly minimized. By arranging the switching pattern such that a significant proportion of the switching transitions occurs when the phase currents and thus the losses are small, the switching losses are kept at the same level as with PWM/SVM, despite the higher switching frequency. Interestingly enough, in terms of switching losses and current distortions, MPDCC with long horizons slightly beats the performance of OPPs—refer to the OPP with pulse number $d = 5$. The torque distortions, however, are worse.

Alternatively, one may wish to minimize the switching losses with regards to PWM/SVM, while keeping the current TDD constant. As an example, consider again PWM with $f_c = 270\,\text{Hz}$. MPDCC with the switching horizon 'eSE', prediction horizon of 63 time-steps and bound width $\delta_i = 0.21$

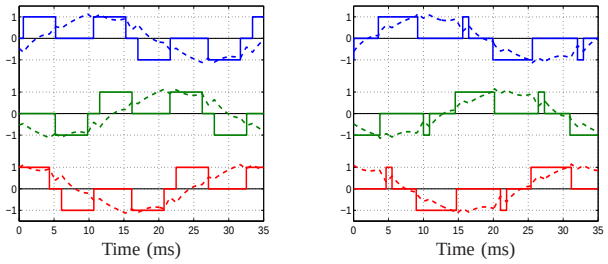

(a) OPP (b) MPDCC

Fig. 9: Comparison of the abc switching patterns of an OPP with $d = 2$, and MPDCC with the switching horizon 'eSE' and the bound width $\delta_i = 0.21$. Both schemes yield the same switching frequency of about 60 Hz

leads to 24% higher current distortions, but the switching losses are reduced from 3.45 down to 1.0 kW, i.e. by 71%! In this case, MPDCC actually outperforms the OPP with pulse number $d = 2$ (44% less switching losses, while the current and torque distortions are very similar). This might appear to be counter-intuitive, since it is often assumed that OPPs provide the upper bound on the achievable steady-state performance of a modulator. Recall that the OPPs were computed by minimizing only the current distortions, not considering the switching losses. By also taking the switching losses into account and by accordingly rearranging the pulses as shown in Fig. 9, MPDCC is able to achieve similarly low distortions, while further reducing the switching losses, see Table III. MPDCC is particularly effective to yield low current distortions, but less effective to reduce the torque distortion, as explained in Sect. IV.

The benefit of MPDCC is particularly pronounced when operating at low pulse numbers. For a switching frequency of about 60 Hz, MPDCC reduces both the switching losses and the current TDD by about 40%, when compared to PWM with the carrier frequency of 90 Hz. For higher switching frequencies, however, the gain is less significant, as demonstrated by the benchmarking with respect to PWM with $f_c = 720$ Hz. This characteristic can be also observed with OPPs, whose performance benefit drops as the pulse number is increased, see Table II.

C. Tuning

In MPDCC, the width of the current bounds is a tuning parameter that sets the trade-off between the level of harmonic distortion and the switching losses. This tuning parameter is

	OPP				MPDCC			
i_a [pu]	-0.65	0.55	0.93	0.93	0.14	1.15	0.33	0.60
E_{on} [J]			0.16		0.02		0.06	
E_{off} [J]	1.48	1.25		2.12		2.62		1.37
E_{rr} [J]	1.94		2.78		0.41		0.99	
$\sum E$ [J]	9.73				5.47			

TABLE III: Switching losses E for the positive halfwaves in phase a shown in Fig. 9. E_{on}, E_{off} and E_{rr} denote the GCT turn-on, GCT turn-off and the diode reverse recovery losses, respectively. MPDCC's switching losses are here 44% less than the ones of the OPP, which is in line with Table II

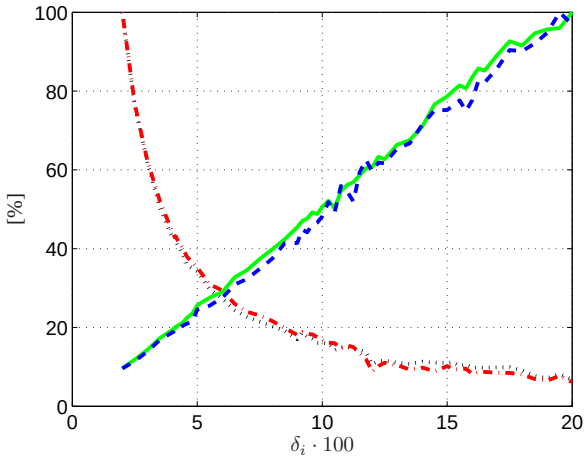

Fig. 10: Tuning of MPDCC: Current TDD (straight green line), the torque TDD (dashed blue line), the switching losses (dash dotted red line) and the device switching frequency (dotted black line) vs the width of the current bound δ_i for MPDCC with the switching horizon 'eSE' at 60% speed and full torque. All four curves are given in percent and normalized to their maximum value in the interval $\delta_i = [0.02, \ldots 0.2]$

equivalent to the carrier frequency in PWM/SVM. Specifically, by tightening the current bounds, the current ripple is reduced and so are the current and torque TDDs. Over a wide range, the relation between the current ripple and the harmonic distortion appears to be linear, as confirmed by Fig. 10.

VII. Conclusions and Discussion

The operation of medium-voltage drives is usually confined to low switching frequencies in the range of a few 100 Hz in order to keep the switching losses low. MPDCC yields very low switching losses for a given level of tolerable current distortions. This also implies that the torque distortions are small. As shown in [25], for the same switching losses and the same switching horizon (computational burden), MPDCC appears to slightly outperform MPDTC in terms of the current distortions. To minimize the torque distortion, however, MPDTC appears to be better suited, see also [25]. The shape of the current ripple sets is responsible for this difference.

At very low switching frequencies, MPDCC achieves switching losses and current distortion levels that are comparable to the ones typically achieved with OPPs. For very low pulse numbers, when approaching six-step operation, MPDCC might even outperform OPPs in this respect.

Long horizons drastically improve the controller performance—short horizons and particularly one-step predictive control, such as [11], appear to be less effective than PWM and SVM, as indicated by [25]. Long horizons are achieved by combining the concept of extrapolation with the notion of imposing bounds on the controlled variables. Yet, when compared to FOC or DTC, the computational burden tends to be high. For short switching horizons, a successful implementation was shown in [15]. To implement long switching horizons, techniques from mathematical programming such as branch and bound can be used, as proposed in [22]. Even though only simulation results

were presented here, the significance of such simulations is underlined by the very close match between the previous simulation results in [14], which were obtained using the same drive model as in this paper, and the experimental results in [15].

In this paper, a three-level NPC inverter was used as a commonly used and illustrative example for a multi-level voltage source inverter. It is a matter of changing the internal controller model and thus a straightforward undertaking to address other topologies and machines. In the case of MPDTC, this simple adaptation was exemplified for five-level topologies [26] and permanent-magnet synchronous machines [27].

ACKNOWLEDGMENT

The author would like to thank Georgios Papafotiou and Frederick Kieferndorf of ABB Corporate Research, Baden-Dättwil, Switzerland for the optimized pulse patterns used as a benchmark and support with the SVM modulator, respectively. A research grant from ABB Corporate Research, Switzerland is gratefully acknowledged.

APPENDIX

The matrices of the discrete-time prediction model (10) are the following.

$$A = \begin{bmatrix} -\frac{1}{\tau_{\sigma'}} & 0 & \frac{k_r}{r_\sigma \tau_{\sigma'} \tau_r} & \frac{k_r}{r_\sigma \tau_{\sigma'}} \omega_r \\ 0 & -\frac{1}{\tau_{\sigma'}} & -\frac{k_r}{r_\sigma \tau_{\sigma'}} \omega_r & \frac{k_r}{r_\sigma \tau_{\sigma'} \tau_r} \\ \frac{x_m}{\tau_r} & 0 & -\frac{1}{\tau_r} & -\omega_r \\ 0 & \frac{x_m}{\tau_r} & \omega_r & -\frac{1}{\tau_r} \end{bmatrix}, \tag{12}$$

$$B_1 = \frac{1}{r_\sigma \tau_{\sigma'}} \begin{bmatrix} 1 & 0 & 0 \\ 0 & 1 & 0 \\ 0 & 0 & 0 \\ 0 & 0 & 0 \end{bmatrix} \frac{V_{\text{dc}}}{2} P\,, \tag{13}$$

$$B_2(x(k)) = \frac{1}{2x_c} x^T(k) \begin{bmatrix} 1 & 0 & 0 \\ 0 & 1 & 0 \\ 0 & 0 & 0 \\ 0 & 0 & 0 \\ 0 & 0 & 0 \end{bmatrix} P^{-T}\,, \tag{14}$$

$$C = \begin{bmatrix} 1 & 0 & 0 & 0 & 0 \\ 0 & 1 & 0 & 0 & 0 \\ 0 & 0 & 0 & 0 & 1 \end{bmatrix}. \tag{15}$$

REFERENCES

[1] K. H. J. Chong and R.-D. Klug. High power medium voltage drives. In *Proc. IEEE Int. Conf. Power Syst. Technol.*, pages 658–664, Singapore, Nov. 2004.

[2] B. Wu. *High-Power Converters and AC Drives*. Intersci. Publ. John Wiley & Sons Inc., 2006.

[3] M. P. Kazmierkowski and L. Malesani. Current control techniques for three-phase voltage-source PWM converters: A survey. *IEEE Trans. Ind. Electron.*, 45(5):691–703, Oct. 1998.

[4] F. Blaschke. A new method for the structural decoupling of ac induction machines. In *IFAC Symp.*, pages 1–15, Oct. 1971.

[5] J. Holtz. Pulsewidth modulation – a survey. *IEEE Trans. Ind. Electron.*, 32(5):410–420, Dec. 1992.

[6] R. Kennel, A. Linder, and M. Linke. Generalized predictive control (GPC) – ready for use in drive applications? In *Proc. IEEE Power Electron. Spec. Conf.*, pages 1839–1844, Vancouver, BC, Canada, 2001.

[7] T. Geyer. *Low Complexity Model Predictive Control in Power Electronics and Power Systems*. PhD thesis, Autom. Control Lab. ETH Zurich, 2005.

[8] D. Q. Mayne, J. B. Rawlings, C. V. Rao, and P. O. M. Scokaert. Constrained model predictive control: Stability and optimality. *Automatica*, 36(6):789–814, Jun. 2000.

[9] A. Linder and R. Kennel. Model predictive control for electrical drives. In *Proc. IEEE Power Electron. Spec. Conf.*, pages 1793–1799, Recife, Brasil, 2005.

[10] S. Mariethoz, A. Domahidi, and M. Morari. Sensorless explicit model predictive control of permanent synchronous motors. In *Proc. IEEE Int. Elect. Mach. Drives Conf.*, pages 1492–1499, Miami, Florida, USA, May 2009.

[11] R. Vargas, P. Cortés, U. Ammann, J. Rodríguez, and J. Pontt. Predictive control of a three-phase neutral-point-clamped inverter. *IEEE Trans. Ind. Electron.*, 54(5):2697–2705, Oct. 2007.

[12] H. S. Patel and R. G. Hoft. Generalized techniques of harmonic elimination and voltage control in thyristor inverters: part I – harmonic elimination. *IEEE Trans. Ind. Appl.*, 9(3):310–317, May/Jun. 1973.

[13] G. S. Buja. Optimum output waveforms in PWM inverters. *IEEE Trans. Ind. Appl.*, 16(6):830–836, Nov./Dec. 1980.

[14] T. Geyer, G. Papafotiou, and M. Morari. Model predictive direct torque control – part I: Concept, algorithm and analysis. *IEEE Trans. Ind. Electron.*, 56(6):1894–1905, Jun. 2009.

[15] G. Papafotiou, J. Kley, K. G. Papadopoulos, P. Bohren, and M. Morari. Model predictive direct torque control – part II: Implementation and experimental evaluation. *IEEE Trans. Ind. Electron.*, 56(6):1906–1915, Jun. 2009.

[16] T. Geyer. Generalized model predictive direct torque control: Long prediction horizons and minimization of switching losses. In *Proc. IEEE Conf. Decision Control*, pages 6799–6804, Shanghai, China, Dec. 2009.

[17] J. C. Ramirez Martinez, R. M. Kennel, and T. Geyer. Model predictive direct current control. In *Proc. IEEE Int. Conf. Ind. Technol.*, pages 1808–1813, Viña del Mar, Chile, Mar. 2010.

[18] S. Mastellone, G. Papafotiou, and E. Liakos. Model predictive direct torque control for MV drives with LC filters. In *Proc. Eur. Power Electron. Conf.*, pages 1–10, Barcelona, Spain, Sep. 2009.

[19] J. Holtz. The representation of AC machine dynamics by complex signal graphs. *IEEE Trans. Ind. Electron.*, 42(3):263–271, Jun. 1995.

[20] P. C. Krause, O. Wasynczuk, and S. D. Sudhoff. *Analysis of Electric Machinery and Drive Systems*. Intersci. Publ. John Wiley & Sons Inc., 2nd edition, 2002.

[21] Y. Zeinaly, T. Geyer, and B. Egardt. Trajectory extension methods for model predictive direct torque control. In *Proc. App. Power Electron. Conf. and Expo.*, Fort Worth, TX, USA, Mar. 2011.

[22] T. Geyer. Computationally efficient model predictive direct torque control. In *Proc. IEEE Energy Convers. Congr. Expo.*, pages 207–214, Atlanta, GA, USA, Sep. 2010.

[23] J. Holtz and S. Stadtfeld. A predictive controller for the stator current vector of AC machines fed from a switched voltage source. In *Int. Power Electron. Conf.*, pages 1665–1675, Tokyo, Japan, Apr. 1983.

[24] B. P. McGrath, D. G. Holmes, and T. Lipo. Optimized space vector switching sequences for multilevel inverters. *IEEE Trans. Power Electron.*, 18(6):1293–1301, Nov. 2003.

[25] T. Geyer. A comparison of control and modulation schemes for medium-voltage drives: emerging predictive control concepts versus PWM-based schemes. *IEEE Trans. Ind. Appl.*, 47(3):1380–1389, May/Jun. 2011.

[26] T. Geyer and G. Papafotiou. Model predictive direct torque control of a variable speed drive with a five-level inverter. In *Proc. IEEE Ind. Electron.*, pages 1203–1208, Porto, Portugal, Nov. 2009.

[27] T. Geyer, G. A. Beccuti, G. Papafotiou, and M. Morari. Model predictive direct torque control of permanent magnet synchronous motors. In *Proc. IEEE Energy Convers. Congr. Expo.*, pages 199–206, Atlanta, GA, USA, Sep. 2010.